Chapter 4
Chirality and Antiferromagnetism in Optical Metasurfaces

Kun Huang

Abstract In this chapter, we will introduce optical chiral metasurfaces that modulate the phase and amplitude of the circularly polarized (CP) light by using orientation-rotated artificial subwavelength structures. For high-efficiency dielectric chiral meta-surfaces, the nanostructures work as nanoscale half-waveplates that hold the physical origins of antiferromagnetism by inducing multiple anti-parallel magnetic dipoles. The interaction between metasurfaces and chiral CP light (carrying the spin angular momentum) enables polarization meta-optics for the applications such as lens, grating and hologram. In addition, the optical vortex beams carrying the orbital angular momentum of light is introduced as another chiral light because the helical wavefronts with opposite handednesses exhibit the mirror symmetry. Such a chiral feature of optical vortex beam is used to probe the chirality of micro-structures, i.e., helical dichroism (HD), which works as a counterpart of circular dichroism (CD) created by the interaction between CP light and chiral molecules. The concluding remarks about the interaction between chiral light and nano-/microstructures are made at the end of this chapter.

4.1 Introduction

Light is a kind of electromagnetic radiation that carries the detectable energy with high oscillating frequencies of hundreds of terahertzs for various usages such as animal vision, illumination and display, information transform, material processing, optical imaging, energy transfer and storage in plants, heating, nano-fabrication, remote sensing and medical surgery. Due to the rich diversity in these applications, the requirement of manipulating light in a highly customized and arbitrary way increases rapidly with the development of modern technology. The fundamental physics of tailoring light is the interaction of light with natural or artificial materials

K. Huang (✉)
Department of Optics and Optical Engineering, University of Science and Technology of China, Hefei, China
e-mail: huangk17@ustc.edu.cn

© Springer Nature Switzerland AG 2021

E. Kamenetskii (ed.), *Chirality, Magnetism and Magnetoelectricity*,
Topics in Applied Physics 138,
https://doi.org/10.1007/978-3-030-62844-4_4

at the different scales ranging from macroscopic bulky crystals, to man-made nanostructures, to microscopic molecules and atoms. Recently, optical metasurfaces made of artificial subwavelength structures has drawn great attention due to its capacity of tailoring the amplitude, phase and polarization of light in a subwavelength thickness. It therefore offers the opportunity to integrate optical elements (Sect. 4.1.1) within a compact volume. The rapid development of optical metasurfaces (Sect. 4.1.2) benefits from matured nanotechnology, which enables the fabrication of optical subwavelength structures. These nanostructures could confine nanoscale resonating modes that behave like electric and magnetic dipoles or multipoles. The electromagnetic resonances of the confined nanomodes are modified through changing the dimension or geometry of the nanostructures, hereby realizing the required modulation of light. Based on these fundamental origins, metasurfaces can be mainly categorized into shape-varied metasurfaces, geometric metasurfaces, Huygens metasurfaces. In this chapter, we only focus on geometric metasurfaces composed of size-fixed orientation-rotated nanostructures that control the phase of circularly polarized light, which carries the spin angular momentum (SAM) of light and exhibits the polarization chirality of light (Sect. 4.2.1). In addition, the orbital angular momentum (OAM) of light carried by optical vortices beams with a helical wavefront (Sect. 4.2.2) characterizes the phase chirality of light. Due to the strong response to the polarization chirality of light, the geometric metasurfaces can also be called as chiral metasurfaces (Sect. 4.3). According to their material platforms, chiral metasurfaces are discussed in terms of plasmonic chiral metasurfaces (Sect. 4.3.1), chiral nanosieves (Sect. 4.3.2), and dielectric chiral metasurfaces (Sect. 4.3.3). In the transmission mode, the dielectric chiral metasurfaces have much higher efficiency than plasmonic metasurfacea and chiral nanosieves, due to the low absorption of dielectrics. In the configuration of dielectric metasurfaces, the nanostructures could support the induced antiparallel magnetic dipoles, implying the antiferromagnetic resonances. Such a concept of antiferromagnetism is used to explain the physics governing dielectric nano-halfwaveplates, which is the functionality of nano-structures in chiral metasurfaces. Finally, the applications of chiral light and chiral metasurfaces (Sect. 4.4) are introduced by addressing the exciting topics such as circular dichroism and helical dichroism (Sect. 4.4.1), and chiral meta-optics (Sect. 4.4.2), followed by a brief conclusion in Sect. 4.5.

4.1.1 Optical Elements

Before 1900, the optical elements such as lenses, glasses, gratings, birefringent crystals, polarizers, mirrors and filters have been well developed with the help of traditional technology of cold machining, thus forming the cornerstone of geometry optics where the dimension is much larger than the operating wavelengths. Light in geometry optics is simplified into a ray of light so that the intensity of an optical beam can be taken as the density of the rays at its cross section. The manipulation of light originates mainly from the refraction and refraction of the ray at the interface between

two media with different refractive indices, where the curvature of the interface and the index difference between two media are the main parameters to tailor the ray of light. The disadvantage of geometry optics comes from the fact that the other variables such as phase, polarization, coherence and diffraction of light are ignored completely due to the model of the ray, so that its applied territory is quite limited.

When the optical elements have the feature size at the level of wavelength, the diffraction and interference dominate its propagation of light and the light-matter interaction due to the wave properties of light. The well-developed lithography enables us to acquire the micro- or nano-scale elements such as optical fibers [1], holograms [2], photonic crystals [3], plasmonic devices [4], optical metamaterials [5, 6] and metasurfaces [7–11], quantum devices, where their feature sizes range from tens of microns to several nanometers. The diffraction effects in micro-devices is weak, which is a good issue for optical fibers during the long-distance propagation. But, the weak diffraction makes micro-pixelated traditional holograms with small field-of-view, leading to the limited applications. Meanwhile, the micro-pixel pitch in traditional holograms allows only the phase and amplitude modulation of light.

When the pixels of devices are below the subwavelength, the polarization effect is important because the subwavelength structures have different electromagnetic resonances for transverse electric and magnetic fields. The photonic crystals with periodic subwavelength pixels could prohibit the motion of photons through confining the electromagnetic modes within the index-contrast structures, hereby creating the forbidden states at the designed frequencies. A well-designed photonic crystal could support the simultaneous oscillation of multiple modes with different polarizations, which is useful to generate the cylindrical vector beams with spatially variant states of polarization in active nanolasers [12]. As its killer-man application, the photonic crystal fibers offer the well-confined modes that are impossible in conventional fibers. However, the periodic properties make photonic crystals incompetent at manipulating the phase of light at the transvers plane vertical to the propagation direction. Such a situation also exists at the periodic meta-materials with the pixel pitches much smaller than one wavelength, where the effective medium theory can be used to approximate its optical properties. For visible light with the wavelengths ranging from 400 nm to 800 nm, the pixel pitches in metamaterials is too small for the state-of-art nanolithography to fabricate a three-dimensional structure, so that the novel properties of metamaterials are frequently demonstrated at the micro-wave and radio frequencies [13].

Fortunately, we can realize two-dimensional meta-materials made of high-refraction-index dielectric or metal-based plasmonic nano-structures with the pixel pitches around a half of wavelength [14], facilitating the fabrication issue by using electron-beam or focused ion lithography. Instead of effective-medium approach in three-dimensional metamaterials, two-dimensional metamaterials have the distinct working principle of controlling the polarization, amplitude, phase and wavelength of light through the electromagnetic responses of the confined nanomodes, which oscillate between two lower-refraction-index media (i.e., substrate and surrounding medium) [15]. Due to its planarity and ultrathin thickness of smaller than one wavelength, two-dimensional meta-materials are usually phrased as “metasurfaces”,

which can be realized easily by using one-step top-down lithography that is a matured technology of manufacturing mass-product integrated circuits in semiconductor industry. Since it could realize full control of light arbitrarily in a compact volume, metasurface-based devices are drawing the increasing attention in integrated opto-electronics and portable devices. Therefore, optical metasurfaces are the main topic that we will focus in this chapter.

From the viewpoint of functionality, the main contribution of optical metasurfaces to optics community is to introduce arbitrary polarization manipulation of light, in addition to amplitude and phase modulation. It allows us to manipulate the local states of polarization at any pixel of interest across an entire meta-device, and simultaneously customize the corresponding amplitude and phase in a high accuracy, which is not possible for all the previous optical elements. For a polarized light, two commonly used orthogonal bases such as linear polarization (i.e., $\mathbf{e}_x$ and $\mathbf{e}_y$, where x and y are the transverse coordinates that are perpendicular to the propagating direction of light) and circular polarization (i.e., $\mathbf{e}_x \pm i\mathbf{e}_y$) can be used to characterize its polarization property. The circular polarization is a simple combination of two orthogonal linear polarizations with an additional phase delay of $\pm\pi/2$, which leads to the rotating vector of electric field in circularly polarized light. Determined by the sign of delayed phase, the rotation is along the clockwise or anti-clockwise direction, which is related with the chirality of light. Optical geometric metasurfaces could transfer a circularly polarized light into its cross-polarization, meanwhile imprint an additional phase that is two times of the rotating angle of the size-fixed rectangle-shape nanorodes. The rectangle nanorodes operate as a miniaturized half-waveplate that provides a phase delay of π between two orthogonal components of electric fields. The mechanism of these half-waveplates depends on the materials: the metal-based plasmonic nano-halfwaveplates hold the physical origin of electric dipole resonances [16], while the high-refraction-index dielectric nano-halfwaveplates originate from the antiferromagnetic resonances [15]. The interaction between chiral light and geometric metasurfaces increases significantly the full manipulation of circular polarized light, and therefore results in many intriguing applications such as polarization meta-optics, spin Hall effects of light [17, 18], beam shaping of chiral light, detection of chirality, which forms the primary configuration of this chapter.

4.1.2 History of Optical Metasurfaces

Ultrathin metasurfaces could full control of electromagnetic waves by using the spatially varied subwavelength structures [11, 13, 14, 19–23] that supports the local responses of well-confined modes, which are commonly used elements at its long-wavelength spectrum. For example, the antennas at the radio and microwave frequencies are designed at the scale of subwavelength for sending or receiving the signals. However, optical metasurfaces have much shorter history because the fabrication and simulation issue of subwavelength structures at the visible or infrared wavelengths cannot be well-solved until the personal computers with powerful scientific

computing capacities are popularized to assist the design and manufacture of optical nano-structures. The first optical metasurfaces were reported in 1998 by Simion Astilean, Philippe Lalanne and their collaborators to demonstrate the blazed gratings with spatially varied subwavelength features of TiO_2 on a quartz substrate at the working wavelength of 633 nm [7, 8]. The phase modulation is controlled by the filling factor of size-varied subwavelength structures in a pixel pitch, with the guidance of effective medium theory. The measured efficiency of 1-order diffraction is 83%, which is slightly larger than the theoretical prediction and indicates a fundamental breakthrough as a novel element. Although further demonstration of meta-lenses is also done with good agreement, the potential of these subwavelength structures has not been fully recognized due to the rough design tools of effective medium theory that ignores the local response of confined nanomodes and the unpolarized illumination that excludes the deep investigation into polarization effects. In addition, the product yield of these devices is lower due to the challenging fabrication at that moment. As a result, these excellent works at their group terminate so that they are not widely exposed among the optics community until recently.

Since 2000, Hasman group reported a series of works that utilized the rotating subwavelength metal or dielectric nanorods to control the phase and polarization of light by introducing the important concept of geometric phase or Berry phase [9, 10, 24–26]. Compared with the size-varied subwavelength structures developed by Philippe Lalanne et al., geometric metasurfaces with size-fixed nanorodes offer much higher level of phase modulation because the geometric phase is determined by the rotating angle of nanorodes without changing their dimension, hereby facilitating the fabrication due to uniformly distributed nanostructures. With this powerful platform of geometric metasurfaces, Hasman group demonstrated many novel devices such as cylindrical vector beams, polarization-dependent hologram and lenses at the infrared wavelengths. These works highlight the significance of subwavelength devices and therefore play an important role in developing and popularizing various optical meta-devices with polarization features. Considering that the dominated electromagnetic resonances existing in geometric metasurfaces were not unveiled clearly at that moment, these metal or dielectric geometric metasurfaces, operating in a transmission mode that is preferred in most optical equipment and systems, were not designed with the suitable geometry and materials, leading to low efficiency for practical applications.

With the rapid development of metamaterials for applications such as perfect lens and electromagnetic cloaking, the interest of utilizing subwavelength structures to control the waves increases quickly among the entire electromagnetic community. The related computing algorithms such as finite-element method (FEM) and time-domain finite-difference (FDTD) method are available at low cost and carried out even at a personal computer, which extremely decreases the threshold of simulating the electromagnetic responses of optical nano-structures. In 2011, Federico Capasso et al. developed size-varied V-shape structures with deep-subwavelength features to tailor the discrete phase of a linearly polarized light (perpendicular to the incident polarization) for blazed gratings and vortex generation at the mid-infrared wavelengths [11]. It offers the first time demonstration of manipulating the phase and

amplitude of scattering light with linear co-polarization, and completely releases the ability of subwavelength structures in shaping the polarized light arbitrarily. The successive works by Capasso group refresh the concept of traditional optics [20, 27–32], which leads to the persistent burst of optical metasurfaces from infrared and visible to ultraviolet regions.

After the consequent development around 10 years, optical metasurfaces, nowadays, have the clear physics that shapes light through the electromagnetic interaction with subwavelength structure in terms of the interference of the confined nanomodes. In theory, we can categorize optical metasurfaces into gradient metasurfaces with sized-varied geometry [11], geometric metasurfaces [16, 33], Huygens metasurfaces [34–36], nanosieve metasurfaces with amplitude modulation [37–40]. The working principle of gradient and geometric metasurfaces have been introduced above. Huygens metasurfaces support the simultaneous resonances of two transversely located electric and magnetic dipoles having the crossed directions and the equal amplitudes, so that every meta-atom or nanostructure in Huygens metasurfaces can be taken as an ideal Huygens point source that has the forward transmission of 1 but the backward scattering of 0, thus offering another strategy of high-efficiency metasurfaces. Photon nanosieves are one kind of amplitude metasurfaces that shapes the binary transmission of light with the etched holes on an opaque thin film. They become the only choice of meta-devices at the extremely short wavelengths such as extreme ultra-violet light and soft-X ray, where all the materials are absorbing [41] so that the electromagnetic resonances of nanomodes cannot exist.

From the viewpoint of structure, optical metasurfaces could utilize the unit cell of any geometric shape for controlling light. The size-varied circular, V-shape and rectangle nano-structures are frequently used in gradient metasurfaces [11, 42], while the orientation-rotated rectangle structures are much preferred in geometric metasurfaces [16, 33] due to the limitation of its mechanism. Optical Huygens metasurfaces frequently adopt the circular dielectric nanodisks to excite the electric and magnetic dipoles [34–36]. Nanosieve metasurfaces generally use the circular or rectangle apertures to modulate the amplitude or geometric phase of light [37–40].

Efficiency of optical metasurfaces is a key parameter for their practical applications in industry. Due to the intrinsic properties of electromagnetic resonances, optical metasurfaces have the efficiency determined mainly by the material platform. The reflective metasurfaces could exhibit the total efficiency of ~90% by using metals or a combination of metallic and dielectric materials with low absorption at the wavelengths of interest [15, 42, 43]. However, the metals are not preferred in an optical transmissive metasurface because of their strong ohmic loss and low polarization conversion [44]. High-efficiency optical metasurfaces in the transmission mode usually uses the refraction-index and large-bandgap dieletric nano-structures sitting on a low-index and transparent substrate, creating a well-confined dielectric nano-cavity that has much higher refractive index than the surrounding environment. This conclusion is valid for all gradient, geometric and Huygens metasurfaces in transmission. Since most of optical equipment and systems work in a transmission mode, optical dielectric metasurfaces with high efficiency are the hotspot among the

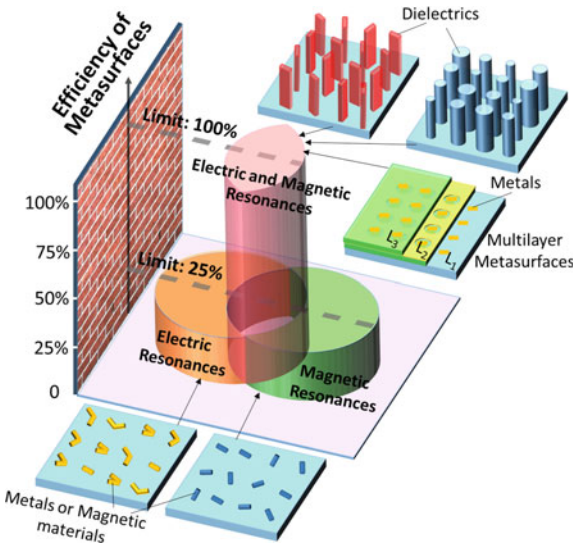

Fig. 4.1 The summary about the efficiency limits of optical metasurfaces. The limit for metasurfaces supporting either electric or magnetic resonance is 25%, while the high aspect-ratio dielectric and multilayer metasurfaces have the efficiency limit of 100%

current metasurface community. To achieve high efficiency, optical reflective metasurfacecs employ the gold (Au) at the near-infrared frequencies, silver (Ag) at the visible wavelengths and aluminum (Al) at the ultrav-violet spectrum, while transmission metasurfaces prefer the silicon (Si) for the near-infrared light, titanium dioxide (TiO_2), gallium nitride (GaN), silicon nitride (Si_3N_4) and gallium phosphide (GaP) for visible light, niobium pentoxide (Ni_2O_5), hafnium dioxide (HfO_2) and diamond for ultra-violet light. Figure 4.1 shows a brief summary about the efficiency limit of optical metasurfaces with electric and magnetic resonances.

Optical devices demonstrated by metasurfaces are frequently called as meta-optics. Compared with traditional optics, meta-optics such as metalenses [33, 45, 46], meta-holograms [37, 38, 43, 44, 47–50], meta-gratings [51–54], beam meta-splitters [55, 56], vortex meta-generators [57, 58], meta-retroreflectors [59], meta-biosensors [60] and image meta-processors [61] have the advantages of compact volume, polarization sensitivity, multiplexing functionality, large degree of freedom, high integration and light weight for portable devices. Benefitting from these novel properties, meta-optics could be used in high-resolution imaging, display, nano-lasing, beam shaping, information recognition, nonlinear optics, quantum physics, bio-sensing, spectroscopy and augmented reality. Note that, this technology of optical metasurfaces is hunting for its killer-man applications where only meta-optics can solve the relative problems so that the meta-devices cannot be substituted by others. Before reaching this goal, we speculate that optical reconfigurable metasurfaces might be the most important issue that should be steadily solved, although many intriguing proposals [62–69] have been reported in a limited or imperfect functionality for the practical usage.

4.2 Chirality of Light

Chirality refers to an object or system cannot be superposed or brought to coincide with itself by its mirror image. It exists in our daily life (left and right hands), physics (spin of a particle), optics (circularly polarized light, optical vortices with opposite topological charge) and chemistry (molecules). The interaction between chiral light and matter dominates the dichromic responses of microscopic particles, molecules and nano-structures, which becomes an efficient tool to detect or characterize the properties of interested objects in both physics and chemistry. Here, the chirality of light and optical metasurfaces and their interactions will be highlighted in this chapter.

4.2.1 Spin of a Photon and Spin Angular Momentum

A circularly polarized (CP) monochromatic light contains two orthogonal components in its vector potential that can be expressed as [70]

$$\mathbf{A} = u(x, y, z)\mathbf{e}^{i(kz-\omega t)} \cdot (\mathbf{e}_x + \sigma i \mathbf{e}_y), \tag{4.1}$$

where the item $\sigma = \pm 1$ denotes the spin or chirality of light, the wave number is $k = \omega/c$, ω is the angular frequency and c is the speed of light in vacuum, $\mathbf{e}_x$ and $\mathbf{e}_y$ are the unit vectors along x and y directions, respectively. Its vector rotates in an anti-clockwise or clockwise way, which is determined by σ. Generally, $\sigma = 1$ indicates the left-handed circular polarized light while $\sigma = -1$ for the right-handed CP light, as sketched in Fig. 4.2. The vectors show the mirror symmetry, implying the feature of chirality. Under the Lorentz gauge, we have the electric and magnetic fields [71]

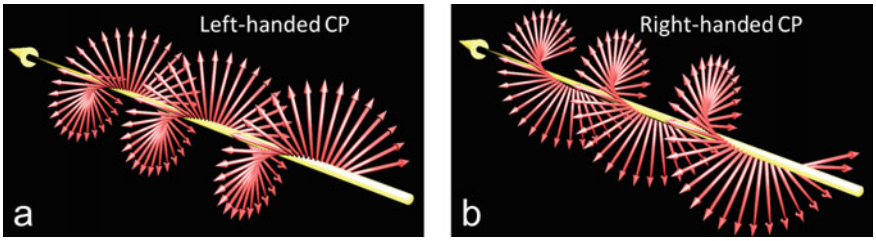

Fig. 4.2 Sketched vectors of electric fields in left- (**a**) /right- (**b**) handed CP light

$$\mathbf{E} = i\omega\mathbf{A} + \nabla\left(\frac{c^2}{i\omega}\nabla\cdot\mathbf{A}\right) = \left[i\omega u\mathbf{e}_x - \sigma\omega u\mathbf{e}_y + c\left(\frac{\partial u}{\partial x} + \sigma i\frac{\partial u}{\partial y}\right)\mathbf{e}_z\right] \exp[i(kz-\omega t), \tag{4.2}$$

and

$$\mathbf{B} = \nabla\times\mathbf{A} = \left[-i\sigma\left(\frac{\partial u}{\partial z} + iku\right)\mathbf{e}_x + \left(\frac{\partial u}{\partial z} + iku\right)\mathbf{e}_y + \left(\sigma i\frac{\partial u}{\partial x} - \frac{\partial u}{\partial y}\right)\mathbf{e}_z\right] \exp[i(kz-\omega t), \tag{4.3}$$

where the paraxial approximation is employed by ignoring the two-order derivations. As suggested by Allen et al., the spin angular momentum (SAM) of a CP Gaussian beam can be evaluated by using [72]

$$\frac{J_z}{W} = \frac{\int\int(\mathbf{r}\times\mathbf{E}\times\mathbf{B})_z r dr d\varphi}{\int\int c\mathbf{E}\times\mathbf{B}_z r dr d\varphi} = \frac{\sigma}{\omega}, \tag{4.4}$$

where only the SAM of light is considered because the Gaussian beam takes no orbital angular momentum (OAM). Equation (4.4) means that the SAM of a photon orientates in the positive or negative z direction, which is labelled by the sign of σ. Light carrying the SAM can be used to control the rotation of an object such as birefringent crystals. More frequently, the CP light with SAMs is used to interact with microscopic chiral molecules that have the distinguished absorption of the left-handed and right-handed light, the phenomena of which is named as "circular dichroism (CD)'. By using circular dichroism, one can distinguish the chirality of molecules that cannot be resolved by using the traditional microscopy due to the diffraction limit. Currently, the CD spectroscopy has been widely used in physics, chemistry and biology.

Generally, the CP light is taken to be chiral because of its unique response to chiral objects. However, the chirality of CP light has not been well understood from the viewpoint of electromagnetic waves until the definition of chirality for electromagnetic waves is defined elegantly by Tang and Cohen [73]. For an electromagnetic wave with the fields **E** and **B**, its chirality is proposed to be expressed by [73, 74]

$$C \equiv \frac{\varepsilon}{2}\mathbf{E}\cdot\nabla\times\mathbf{E} + \frac{1}{2\boldsymbol{\mu}}\mathbf{B}\cdot\nabla\times\mathbf{B}, \tag{4.5}$$

where ε and μ are the permittivity and permeability of the surrounding medium. After introducing (4.2) and (4.3) into (4.5), we have its chirality $C = \sigma\varepsilon k\omega^2 u^2$, which is related with the spin σ and the intensity density u^2 at the position of interest. Therefore, (4.5) is also referred as the local chirality density. Once the CP light interacts with the plasmonic structures, the local intensity might be much higher

than the incident light due to the enhancement of local electric fields, leading to a larger C than $\sigma\varepsilon k\omega^2 u^2$. Such a phenomena is named as superchiral, which is also found in the standing waves generated by the interference between two beams with the equal amplitude and opposite propagating directions. Although the superchiral phenomena can enhance the CD response, the value of CD is still located at the level of micro-degrees when the CP light is used to detect the molecules. The possible reason might come from the mismatch between the dimension of molecules and the operating wavelength of light. In contrast, the interaction between the CP light and the subwavelength structures in optical metasurfaces is quite strong so that it can be used to induce the giant spin Hall effects of light [13] or demonstrate the spin-dependent meta-optics [44] (see more details in Sect. 4.2). In addition, it has been recently discovered that the topological structure of the CP light plays an important role in enhancing the CD responses because the symmetry of the beam is changed when the optical vortices with helical wavefronts are introduced [75].

4.2.2 *Optical Vortices and Orbital Angular Momentum*

Beams carrying a helical wavefront exhibit the vortex-like energy flow, alike the case of vortices in water, and therefore are called optical vortex beam. The paraxial vortex beams such as Laguerre-Gaussian and Bessel beams have the singularities at their centers. Along the arbitrary closed curve containing the singularity, the accumulated phase difference divided by 2π is an integer of l, which is the topological charge of optical vortices and corresponds to the topological feature such as the self-healing effects. Thus, an optical vortex beam takes an angle-dependent phase profile of $e^{il\varphi}$, which generates the helical wavefront and the axis-symmetry doughnut-shape intensity profile (see Fig. 4.3). In 1992, Allen et al. found that such kind of optical vortex beams under the paraxial approximation have the orbital angular momentum

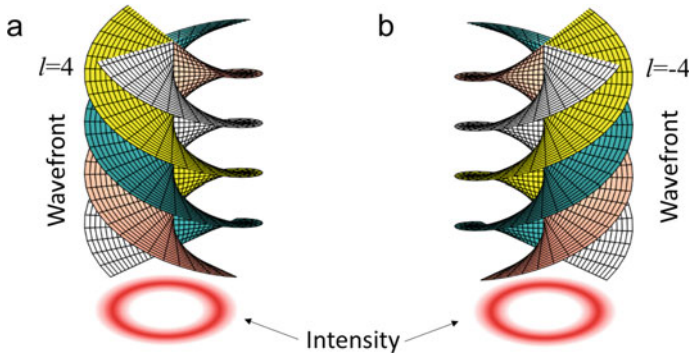

Fig. 4.3 Intensity and phase profiles of optical vortex beams with the opposite-handedness wavefronts: $l = 4$ (**a**) and $l = -4$ (**b**)

of $l\hbar$ per photon, where $\hbar$ is the reduced Planck constant [72]. It thus connects the microscopic quantity of OAM with the macroscopic phase profile of $e^{il\varphi}$. The mathematical proof of the OAM carried in optical vortex beam can be found easily by using a circularly polarized Laguerre-Gaussian beam with its vector potential of $\mathbf{A} = u(r,z)\mathrm{e}^{il\varphi}\bullet\mathrm{e}^{i(kz-\omega t)}\bullet(\mathbf{e}_x+\sigma i\,\mathbf{e}_y)$, where the amplitude part is angle-independent, r and φ are the polar coordinates. The Lorentz gauge yields the similar electric and magnetic fields in (4.2) and (4.3) after $u(x, y, z)$ is substituted by $u(r, z)\mathrm{e}^{il\varphi}$. By using (4.4) under the paraxial approximation, we have the total angular momentum

$$\frac{J_z}{W} = \frac{l+\sigma}{\omega}, \tag{4.6}$$

where the spin item σ refers to the SAM of the circular polarized light and l is related with the OAM of light. For a linearly polarized vortex beam, its SAM is zero, leaving the OAM of $l\hbar$ per photon. Considering that the OAM of light is a microscopic variable, optical vortices with the OAM has been intensely investigated in quantum physics. From the helical phase profiles, one can find that the orthogonality between two arbitrary OAM states is extremely good, so that it can be used for the purpose of communication. In quantum entanglement [76] and optical communication [77–79], the OAM channel could provide the low crosstalk for high-fidelity data transmission. Meanwhile, because the integer l can take any value, the number of OAM channels in communication is unlimited, which therefore could increase the capacity of data transmission.

As denoted in (4.6), the OAM in an optical vortex beam can take the positive or negative value, which presents its direction of z or –z, respectively. It means that the energy flow in the vortex beam moves clockwise or anti-clockwise, behaving like the spin of a photon in a CP beam. When a tightly focused OAM is used to trap the micro-particles within the ring-shape intensity, the OAM of the photons is transferred to micro-particles, leaving a clockwise or anti-clockwise moving trajectory that is determined by the sign of l. All these phenomena suggest the chiral behavior of optical vortices, which is therefore expected to have the strong interaction with chiral objects. However, a plethora of theoretical and experimental works show no obvious interaction with chiral molecules [80]. The rigorous theory proves that the OAM states can respond to the electric quadrupole excited in molecules [81], but its corresponding excitation rate is extremely low in real world. With the help of unique nanoparticle aggregates that could excite the electric quadrupole efficiently, a recent work has reported the first observation of discriminating two chiral enantiomers by the optical vortices with opposite topological charges [82]. Note that, since the electric quadrupoles are excited by the third part, the resulting scattering induced by two vortices has the little difference, leading to a quite weak helical dichroism (HD) of 0.8% [82]. From the viewpoint o practical applications, such a tiny HD cannot be used to detect the chirality of objects in a steady way. More efforts should be made to enhance the HD for the wide usage. An experimental attempt to solve the problem [83] is provided under the theoretical consideration in Sect. 4.4.

4.3 Optical Chiral Metasurfaces

As introduced in Sect. 2., optical metasurfaces contain many types of structures that are employed to control light with different polarizations. Considering the limitation of the topic about chirality, we constrain ourselves to discuss the chiral metasurfaces that manipulate the circularly polarized light with the geometric phase. All the chiral metasurfaces follow the same mechanism of realizing the geometric phase. We start by giving a universal introduction about geometric metasurfaces containing the birefringent nanostructures that have different responses to two orthogonal components of an incident circularly polarized light. Without the loss of generality, we define the scattering Jones matrix of the non-rotating nanostructure by using $S(\varphi = 0) = \begin{bmatrix} s_x & 0 \\ 0 & s_y \end{bmatrix}$, where the scattering factors $s_x$and s_y stand for the complex modulation of x- and y-components of the incident polarized light, respectively. The anti-diagonal elements are fixed to zeros under the assumption that the optical scattering by the nanostructures will not generate a new electric component orthogonal to the incident one, which is usually valid for rectangle-shape nanostructures. If the nanostructure has a rotating angle of φ with the x-axis, its scattering matrix is

$$\mathbf{S}(\varphi) = \mathbf{R}(-\varphi)\begin{bmatrix} s_x & 0 \\ 0 & s_y \end{bmatrix}\mathbf{R}(\varphi) \tag{4.7}$$

where the rotation matrix $\mathbf{R}(\varphi) = \begin{bmatrix} \cos\varphi & \sin\varphi \\ -\sin\varphi & \cos\varphi \end{bmatrix}$. When a circularly polarized beam with the electric field of $\mathbf{E}^{\sigma} = E\bullet(\mathbf{e}_x + \sigma i\mathbf{e}_y)$ is incident on the nanostructure, the scattering light has the electric field

$$\begin{aligned} \mathbf{E}_s &= \mathbf{S}(\varphi)\mathbf{E}^{\sigma} = E\begin{bmatrix} \cos\varphi & -\sin\varphi \\ \sin\varphi & \cos\varphi \end{bmatrix}\begin{bmatrix} s_x & 0 \\ 0 & s_y \end{bmatrix}\begin{bmatrix} \cos\varphi & \sin\varphi \\ -\sin\varphi & \cos\varphi \end{bmatrix}\begin{bmatrix} 1 \\ \sigma i \end{bmatrix} \\ &= \frac{s_x + s_y}{2}\mathbf{E}^{\sigma} + \frac{s_x - s_y}{2}e^{2i\sigma\varphi}\mathbf{E}^{-\sigma}, \end{aligned} \tag{4.8}$$

where $\mathbf{E}^{\pm\sigma} = E\bullet(\mathbf{e}_x \pm \sigma i\mathbf{e}_y)$. In (4.8), the left item refers to the co-polarized part that is usually taken as the background in the scattering light, while the right one implies that the scattering light contains a cross-polarized part with an additional phase modulation of $e^{2i\sigma\varphi}$. Such geometric phase depends on both the chirality of incident light and the rotating angle φ of the nanostructures. It means that the geometric metasurfaces respond to the chiral part in a polarized light, which is therefore named as chiral metasurfaces in this chapter. In addition, the geometric phase arises from the rotation of spatial coordinates, which is thus valid for any birefringent nanostructures (such as chiral metasurfaces and the molecules of liquid crystal) or bulky crystals (such as half-waveplates).

For optical chiral metasurfaces, the total scattering $\mathbf{E}_s$ can be tuned by controlling the parameters s_x and s_y, which are determined by the geometry of nanostructures, materials and working mode. In (4.8), the item $|s_x - s_y|/2$ is related with the efficiency of metasurfaces. For the passive nanostructures without gain, we have $|s_x| \leq 1$ and $|s_y| \leq 1$. To achieve high efficiency, one should maximize $|s_x - s_y|/2$ and minimize the co-polarization part $|s_x + s_y|/2$. Mathematically, the highest conversion efficiency is 1 by setting $s_x = -s_y = 1$, which means that the nanostructures have the equal amplitude of 1 and the phase delay of π between two orthogonal components of the scattering light. Correspondingly, the conversion efficiency is 0 when $s_x = s_y$, implying that the nanostructures have the isotropic responses for the E_x and $E_y$polarized light. The zero-efficiency case usually appears in the circular and square nanostructures. Therefore, most of the demonstrated geometric metasurfaces adopt the nanostructures with anisotropic geometry, such as rectangle shape. On the basis of working principles, they are classified into plasmonic chiral metasurfaces, helical nanosieves, and dielectric chiral metasurfaces, where the nano-structures work as miniaturized half-waveplates that holds the physical origins of electric dipole resonances, birefringent transmission and antiferromagnetic resonances, respectively. In practical design of nanostructures, one tune the parameters s_x and s_y that are controlled by the geometry of nanostructure for a give material platform and numerically simulated with the help of electromagnetic numerical calculation methods such as finite-element method (FEM) and finite-difference time-domain (FDTD) methods. Both electromagnetic simulation methods are important in designing optical metasurfaces and the relative sources can be found easily, so that we will not introduce them here.

4.3.1 Plasmonic Chiral Metasurfaces

Figure 4.4 sketches plasmonic chiral metasurfaces in a transmission and reflective mode. The working principle is the anisotropic resonances of the electric dipoles induced by the circularly polarized incident light. With the illumination by the circular polarized light, the metal nanorodes have the plasmonic resonances at the designed wavelengths. Considering that the feature size of nanorode is smaller than one wavelength, the plasmonic resonances induced by E_x and E_y components could be approximated theoretically as optical responses of two electric dipoles orientated along x and y directions, respectively. For the transmission mode as shown in Fig. 4.4a, the single-layer nanostructures can excite the transversely located electric dipoles that have both the forward and backward radiation. But, only the forward radiation is useful for controlling the s_x and s_y parameters, which refer to the transmittance r_x and r_y in the transmission mode. In addition, due to small filling factor of nanostructures, most of the incident light has no any interaction with nano-structures and directly passed through the substrate, leaving the background with co-polarization in the transmitted light. Therefore, the transmissive plasmonic chiral metasurfaces have the low conversion efficiency. The rigorous electromagnetic theory predicts that the highest conversion efficiency is 25% for metasurfaces that support only electric

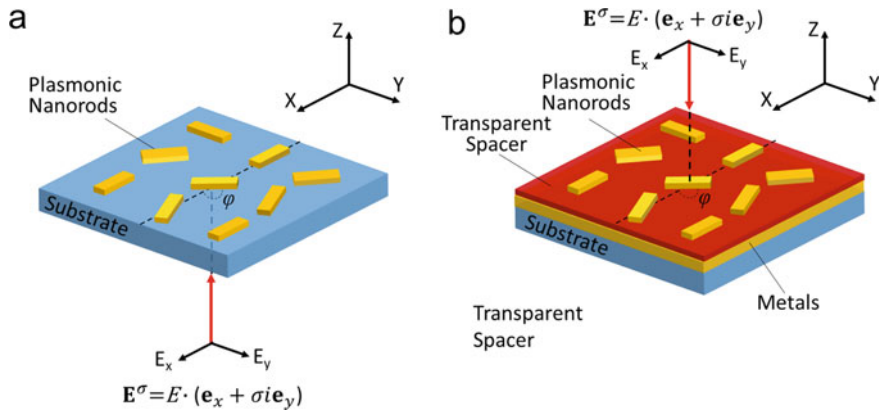

Fig. 4.4 Sketch of plasmonic chiral metasurfaces working in the transmission (**a**) and reflective (**b**) mode

or magnetic resonances [84], while the efficiency limit is 100% if both electric and magnetic resonances exist in the nanostructures [85]. In this transmissive plasmonic chiral metasurfaces, only the electric dipoles are excited, implying its theoretical limitation of 25% in the transverse efficiency.

To enhance the efficiency, the reflective plasmonic chiral metasurfaces have been proposed as shown in Fig. 4.4. In this configuration, the reflective metasurfaces are composed of a single-layer nanostructures, a transparent spacer and a single-layer high-reflectivity metal film on the substrate. Although the plasmonic resonances are similar with the transmission case, the reflective architecture allows two-time interaction between light and nanostructures during the incidence and reflectivity of light. Equivalently, the reflective metasurfaces behave like two-layer meta-materials with the same top and bottom nano-structures, which are separated by the transparent spacer with twofold thickness. The area of transparent spacer sandwiched by the metallic nanostructures and films allows for the magnetic resonances that are induced by the electric responses. Figure 4.5 shows the simulated intensity profiles of such reflective metasurfaces, where the metal is gold and the transparent spacer is made of silicon dioxide (SiO_2). One can clearly observe that both electric and magnetic dipoles oscillate in a unit cell, which offer much higher conversion efficiency of 80% at the visible wavelengths [43]. Such a conclusion implies that, the chiral metasufaces working in a transmission mode could also provide high conversion efficiency if the magnetic dipoles are also induced by constructing a three-dimensional metal-ring structure, which is, however, challenging to be fabricated due to the small footprint of hundreds of nanometers for optical metasurfaces.

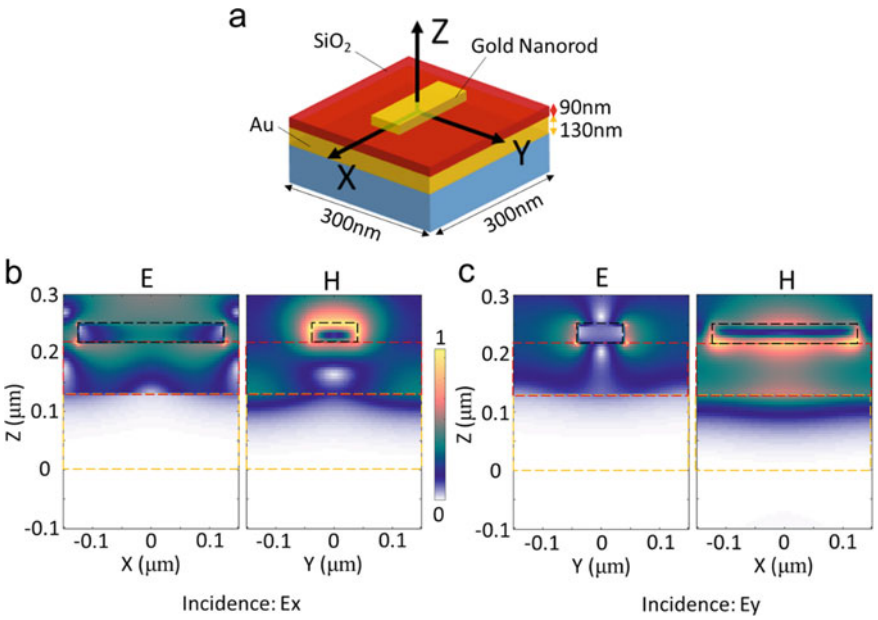

Fig. 4.5 Electric and magnetic fields of scattering light by the reflective plasmonic chiral metasurfaces. The reflective chrial metasurfaces are composed of an 80 nm * 250 nm * 30 nm gold nanostructure, a single-layer SiO_2 film of 90 nm thickness and a reflective gold film of 130 nm on a quartz substrate, as sketched in (**a**). The simulated electric and magnetic fields under the illumination of E_x and E_y polarization are provided in (**b**) and (**c**), respectively

4.3.2 Chiral Nanosieves

Photon sieves are the etched micro-apertures on an opaque film and have been proposed to control light in 2001 due to their advantages of suppressing the side-lobes of a focal spot in optical focusing [86]. In 2015, this concept of photon sieves was introduced into nano-optics by using the nano-apertures, i.e., nanosieves [37], which were used as one kind of typical amplitude metasurfaces to generate a tight spot beyond the diffraction limit and construct a high-uniformity ultra-broadband holographic image [38]. The interference between the diffracted light from these nanosieves will yield the expected intensity profiles by optimizing the locations of nanosieves. Since these nano-apertures is subwavelength, the vector features of diffracting light by them must be taken by using vector electromagnetic analysis that combines the coupled-mode theory and the multipole expansion, yielding an analytical solution of optical diffraction by a circular hole [37]. Due to the axis-symmetry feature, the circular nanosieves have no any dependence on the polarization of incident light, which is good for robust manipulation of arbitrarily polarized light. On the other hand, the circular nanoiseves lose the polarization and phased degree of freedom during the manipulating of light. So, the rectangle nanosieves are proposed

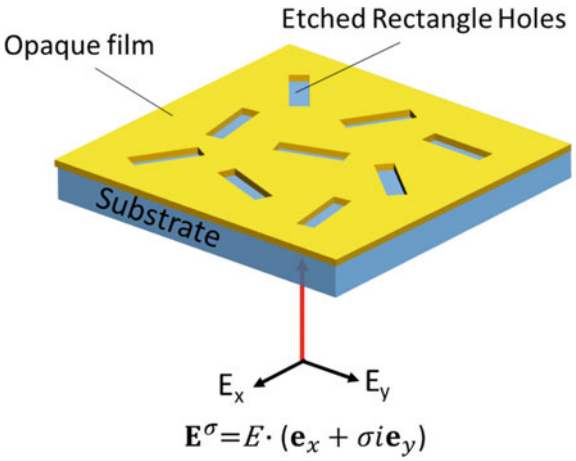

Fig. 4.6 Sketch of chiral nanosieves that contains the rectangle holes etched on an opaque film

to shape the amplitude, phase and polarization of light simultaneously [39, 87]. Here, we just discuss the chiral nanosieves with rotating rectangular apertures, which can be used to control the chiral light that is focused in this chapter.

Figure 4.6 shows the sketch of chiral nanosieves that work in a transmission mode. In appearance, the chiral nanosieves are the complementary structures of transmissive plasmonic chiral metasurfaces (Fig. 4.4a). But, the working principle of chiral nanosieves depends on the anisotropic transmission of *x*- and *y*-polarized light, that is, the parameters s_x and s_y refer to t_x and t_y that are mainly determined by the dimension of the hole. It means that the plasmonic resonances are not mandatorily required in chiral nanosieves, which holds the significant difference from the transmissive plasmonic chiral metasurfaces. Such a fundamental difference makes the chiral nanosieves more useful than plasmonic chiral metasurfaces because the plasmonic resonances are absent at the short-wavelength electromagnetic waves such as extreme ultraviolet light and soft-X rays, where all the materials are absorbing [40]. Thus, the chiral nanosieves become the good candidate to shaping the spin of EUV and soft-X photons in an easier way than the traditional reflective [41] and refractive [88] elements. The recent experimental results have revealed that the phase modulation of chiral nanosieves is valid in the absence of plasmonic resonances [40]. The conversion efficiency of chiral nanosieves is around 0.4% without plasmonic resonances, which confirms the feasibility of manipulating the EUV and soft-X photons by using chiral nanoisieves. In comparison with some high-efficiency elements, the chiral nanosieves are incompetent at the visible frequencies.

4.3.3 Dielectric Chiral Metasurfaces and Anti-ferromagnetic Resonances

Both transmissive chiral metasurfaces mentioned above cannot obtain high conversion efficiency. According to (4.8), high-efficiency chiral metasurfaces should maximize s_x and s_y, which is determined by the simultaneous oscillation of electric and magnetic nanomodes. For the plasmonic chiral metasurfaces and chiral nanosieves, both resonances cannot be satisfied due to either the single-layer induced electric responses or the strong ohmic loss of metallic materials [44]. In addition, the phase delay of π between s_x and s_y should also be met to realize the polarization conversion, and any deviation from π will lead to the existence of co-polarized light even if both s_x and s_y approaches 1. Although the reflective plasmonic chiral metasurfaces [43] offers high conversion efficiency that can only be checked by numerical simulations, it is difficult to explain the fundamental reason of generating the phase delay of π, which is usually ignored in most literatures. In addition to the reflective plasmonic chiral metasurfaces, dielectric chiral metasurfaces could also generate high conversion efficiency by employing the low-loss and high-refractive-index high-aspect-ratio dielectric nanostructures, which support the simultaneous electric and magnetic dipoles [35]. The magnetic dipoles are generated by the induced circle-shape electric displacements with alternating handedness. Thus, both resonances of electric and magnetic dipoles promise the large s_x and s_y that approach 1. Due to the high refractive index, the effective wavelength in dielectric nanostructures is much smaller than the vacuum wavelength, thus allowing multiple electric and magnetic dipoles in nanostructures. It leads to the existence of antiferromagnetic modes that contain a series of vertically locate antiparallel magnetic dipoles [15], which holds the fundamental physics of generating the phase delay of π.

By following our previous work about ultra-violet dielectric chiral metasurfaces, we will discuss the roles of antiferromagnetic nanomodes [15]. Figure 4.7 plots the sketch of the chiral metasurfaces and their optical performance with the simulated efficiency as high as 80% at the designed wavelength of 355 nm. The material of niobium pentoxide (Nb_2O_5) offer high refractive index of 2.2 and low absorption at the wavelengths ranging from 350 nm to 400 nm, hereby enabling the ultraviolet metasurfaces. To reveal the underlying physics, we investigate the detailed electromagnetic responses of dielectric chiral metasurfaces with the maximum conversion efficiency of 80% when the nanostructure has the dimension of L = 150 nm, W = 70 nm and H = 430 nm.

Figures 4.7d, e show the simulated electric and magnetic fields induced by $E_x$and E_y components of the incident polarized light. For E_x component in Fig. 4.7d, the induced electric displacements contain four alternative circular currents in clockwise and anti-clockwise directions, which could generate the relative antiparallel magnetic dipoles (AMPs) sitting vertically along z axis. This staggered magnetization has the similar behavior with one-dimensional antiferromagnetic chain, which has recently been reported in plasmonic nano-disks and hybrid metamaterials. The antiferromagnetic modes have the even electric circle-shape currents with alternative directions,

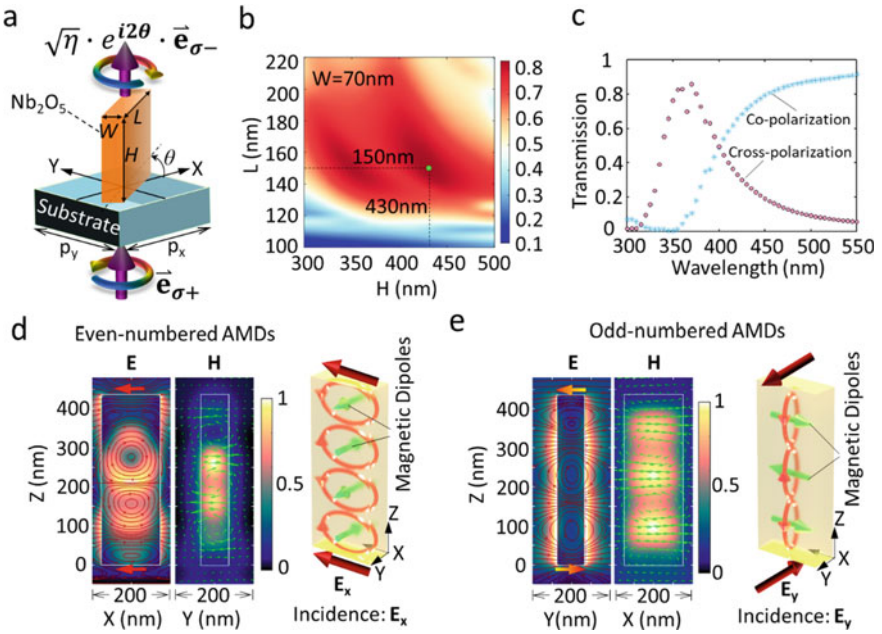

Fig. 4.7 **a** Sketch of dielectric chiral metasurfaces that use Nb_2O_5 to manipulating the ultraviolet light. **b** The simulated conversion efficiency of Nb_2O_5-base chiral metasurfaces at the interested wavelength of 355 nm. Considering the limitation of fabrication issue, the width is set to be 70 nm. The simulation is carried out by scanning the length and height of nanostructures with the help of FDTD methods. **c** The broadband response of the optimized nanostructures with W = 70 nm, L = 150 nm and H = 430 nm. **d**–**e** The simulated electric and magnetic fields under the illumination of E_x and E_y-polarization light. The inserts show the simplified sketches of magnetic dipoles. Reproduced with the permission from 2019 WILEY-VCH Verlag GmbH [15]

which thus enable the same orientation of both the electric vectors at the bottom and top ends of nanostructure (see Fig. 4.7d). It means that the *x*-component of CP light is not changed after the electromagnetic interaction with nanostructures. However, for E_y component, the antiferromagnetic mode is induced with three AMPs, leading to the odd circular currents that could reverse the electric vector of light at the terminal of transmission, as observed in Fig. 4.7e. It indicates a phase delay of π, which is desired for realizing high conversion efficiency. As a result, the transmitted light has the orthogonal polarization to the incident light, which is highly deserved in high-efficiency meta-devices [15]. Figure 4.8 sketches the details during the entire optical process intermediated by antiferromagnetic modes during the realization of circular polarization conversion into its cross-polarization.

Two coupling effects dominates the electromagnetic interaction between the oscillating nanomodes and the designed nanostructures [15]. Firstly, the number of the reduced magnetic dipoles in the antiferromagnetic nanomode is determined by the coupling between the volume modes and the dimension of nanostructures. Along the long axis (i.e., *x* axis) of nanostructures, the volume of magnetic dipole moments is

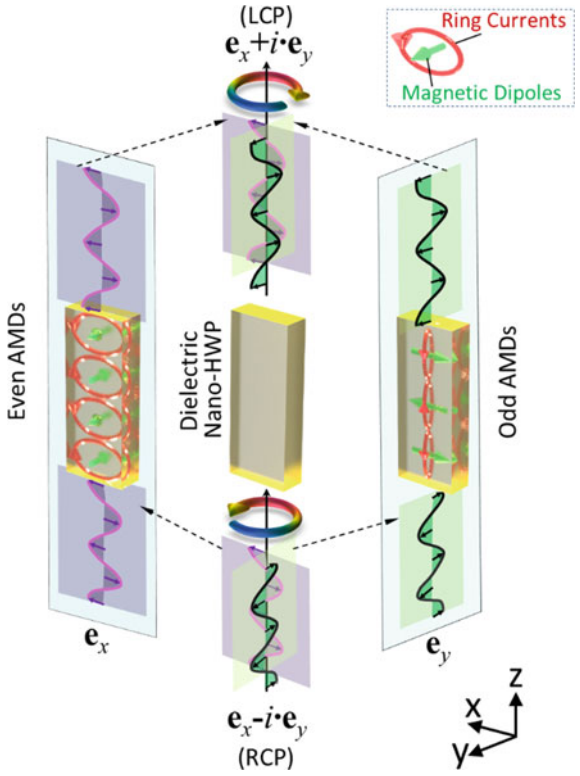

Fig. 4.8 Working principle of antiferromagnetic modes in realizing the polarization conversion

larger than the *y*-orientated magnetic dipoles. The limited volume of a nanostructure leads to the fact that, y-orientated magnetic dipoles are larger than the x-orientated ones, leading to the even and odd AMPs for realizing the phase delay of π. Secondly, every magnetic dipole coupled in an identical antiferromagnetic mode will compete, leading to the different magnetic momenta that influence the total magnetic field [15].

4.4 Applications of Chiral Light and Metasurfaces

In this section, we will discuss the applications of chiral light and chiral metasurfaces in various fields such as detecting the chirality of microscopic objects, optical spin Hall effects and polarization meta-optics.

4.4.1 Circular Dichroism and Helical Dichroism

In chemistry and biology, many molecules have the same compound of different atoms but are assembled with different chirality, which can be distinguished by their circular dichroism (CD) spectroscopy that measures the absorption difference of the right-handed and left-handed circularly polarized light over a wide range of wavelengths. The fundamental physics is that, the chiral enantiomers have the different extinction coefficients for right- and left-handed circular-polarization light. The CD topic has been discussed in many literatures and therefore is ignored here, so that we can focus the detection of chirality by using another chiral light with orbital angular momentum as introduced in Sect. 3. The OAM-based chiral detection draws the increasing attention because the traditional CD spectroscopy has the disadvantages of the weak CD responses at the level of micro-degrees and the broadband illumination, which imposes the requirement on the optical detectors and the lasers.

One of our recent works has addressed the issue about OAM-based chiral detection of micro-objects [83], as sketched in Fig. 4.9. Since the beams carrying the OAM of light have the doughnut-shape intensity profile, the light-matter interaction happens in a ring of intensity profile, where the energy of photons flows along a helical trajectory of micro-sized radius under the tightly focusing condition. It determines the interacting dimension of OAM at the level of microns. It is different from the spin of a circularly polarized light which the chirality of the photon is local at the cross section of entire beam, implying that a spinning photon has strong interaction dimension at the level of operating wavelengths. Therefore, we infer that the OAM can be used to detect the chirality of micro-sized objects. Figure 4.9 sketches the interaction between optical vortices and chiral micro-objects. Due to the helical wavefront of optical vortices, the incident angle generated by two optical vortices with opposite topological charges is different as illustrated in Fig. 4.9, leading to the differential reflectivity between these two optical vortices. During this procedure, the polarization issue is ignored so that we can define the differential scattering induced by OAM as [83]

$$\mathbf{VDS} = \frac{R_{l,s} - R_{-l,s}}{(R_{l,s} + R_{-l,s})/2}, \tag{4.9}$$

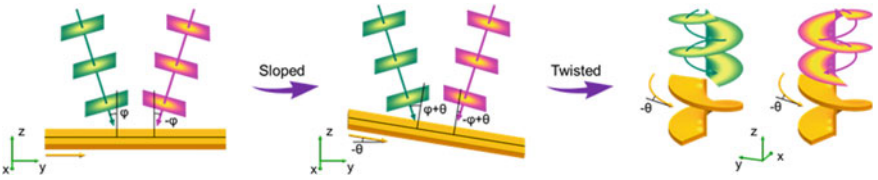

Fig. 4.9 Working principle of OAM-based chirality detection

where R is the optical reflectivity, l denotes the topological charge of optical vortices, the spin s of the incident beam is set to be identical for avoiding the CD effect. The definition of vortical differential scattering (VDS) emphasizes the importance of optical vortices by evaluating the OAM-induced dichroism between the topological-charge-opposite vortices. We have to emphasize that, the VDS has the fundamental difference from CD, because the VDS refers to the scattering difference between two chirality-opposite vortices while the CD comes from the difference of absorption to both circularly polarized light [83].

Based on the definition of VDS, the experimental setup is proposed to characterize the reflectivity difference induced by the chirality-opposite vortices [83]. A femtosecond laser with linear polarization is used here to generate the chirality-opposite optical vortices with a spatial light modulator. The optical vortices are focused by a high numerical aperture objective lens and then illuminate the chiral microstructures. The scattering signals that reflect from the chiral microstructures are collected by the focusing objective lens and later recorded by a CCD camera. The achiral structure of circular disk is used as a control of experiment. The recorded signals at the different topological charges of $|l|$ clearly shows the difference between the optical vortices with the opposite wavefronts (RHW and LHW) for the chiral micro-structures. In comparison, the controlled experiment gives nearly the same reflectivity from both optical vortices. All these experimental observations have suggested that the optical vortices with opposite topological charges can be used to distinguish the chirality of micro-structures due to the difference of the scattering light. To check its VDS further, we carried out the numerical calculation by using the experimental data. It exhibits that the VDS is positive for left-handed structures, negative for right-handed structures and zero for achiral structures. It gives the proof that the chirality of microstructures has been discriminated by using VDS, which therefore provides another method of detecting the chirality of objects in addition to the traditional CD spectroscopy [83].

Compared with CD method, the VDS has the following properties. Firstly, VDS operates at a single wavelength, and therefore releases the requirement of broadband sources in CD spectroscopy. Secondly, the strong VDS happens when the micro-structures have the dimension larger than the operating wavelength. Such a feature is determined by the large interacting area of optical vortices due to the doughnut-shape intensity profiles. Thirdly, the topological charges of optical vortices are unlimited so that it provides the infinite dimension of chiral OAMs, implying that the VDS has much larger degree of freedom than the CD with two spins of photons in a circularly polarized light [83].

4.4.2 Chiral Meta-Optics

By using (4.8), one can find that the arbitrary manipulation of chiral light could be realized by customizing the spatially varied phase profiles to meet the special requirement in practical applications. Here, we introduce three kinds of phase profiles

to demonstrate lenses, holograms and gratings for optical imaging, vectorial holographic anticounterfeiting and beam splitter. In addition, when illuminated by a linearly polarized beam, the chiral metasurfaces will induce the spin-dependent shifts of beam centroids, which is usually related with the spin Hall effects of light [17].

I. Metalenses and imaging

To realize a focusing spherical-aberration-free lens by using chiral metasurfaces, the phase profiles have the function of [33, 46, 89]

$$\phi(x, y) = \frac{2\pi}{\lambda}\left(f - \sqrt{r^2 + f^2}\right), \tag{4.10}$$

where f is the focal length of the lens, $r^2 = x^2+y^2$, λ is the wavelength. Correspondingly, the rotation angle of every nanostructure is $\varphi(x, y) = \phi(x, y)/2$. From (4.8), we can see that the real focusing length depends on the spin of the incident circularly polarized light. It means that a metalens with the phase profile in (4.10) can offer the convergent or divergent functionality, which can be switched by changing the spin of incident light.

The focusing spot generated by such a metalens gives the Airy-like intensity profile that obeys the diffraction limit of 0.515λ/NA [46], where NA is the numerical aperture of the metalens. Therefore, the metalens can give the diffraction-limited imaging, which, however, suffers from the off-axis and achromatic aberrations. The off-axis aberration has been solved by a meta-doublet. One singlet is responsible for the aberration correction [90] and the other is used to realize the functionality of focusing. To solve the achromatic aberration, the hybrid nanostructure [91] or ultrahigh aspect-ratio dielectric nanorod [89] has been proposed and demonstrated experimentally in a low-NA lens, which behaves better than the uncorrected metalens. However, it should be noted that the aberration is much more severe in a high-NA lens than the low-NA one. Especially, a high-NA metalens has a phase cycle of 2π over the radial distance of one wavelength at the outmost rings. Since the pixel pitch of current metalens is around half a wavelength [46], there is only two nanostructures along the radial direction of the metalens so that the aberration cannot be eliminated completely.

II. Meta-gratings and beam splitters

Benefitting from the subwavelength pixel pitch, the chiral meta-gratings usually have the form of blazed gratings with a linearly varied phase. Similarly, a circularly polarized light passing through the metagratings deflects in one direction, while the opposite-spin light runs out in the other direction. When a linearly polarized light works as the incident light, these both deflecting beams can be generated with different spins, which refers to the spin Hall effects of light [92]. It means that the chiral meta-gratings can be used to filter out the spin components of a polarized light. If the chiral meta-gratings are combined with the linear-polarization metagratings, the

diffracted beam could contain four parts: two orthogonal linear-polarization components and two spin components, which can be used to reconstruct the state of incident polarization. It holds the working principle of a metasurface-based polarimetry [54].

III. Chiral meta-holograms and vectorial anticounterfeiting

If the encoded phase profile in (4.8) is used to generate a holographic image, such a metasurface is called as meta-hologram that is different from the traditional holograms. Due to the distinct polarization response in a subwavelength pixel, the chiral meta-holograms could generate the spin-dependent or vectorial images in a large angle-of-view, without the high-order diffraction and twin-image issues that exists in the traditional holograms. For a chiral meta-hologram, the generated image also has a spin-dependent behavior. If the chiral meta-hologram works in a Fresnel distance, it will generate a real holographic image along the propagating direction of the circularly polarized incident light with one spin but form a virtual image for the other spin [44]. However, a Fraunhofer metahologram illuminated by the circularly polarized light with both spins will create the real images with center-symmetry properties [49]. Both Frensnel and Fraunhofer metaholograms have been experimentally demonstrated with the good agreement.

In fact, both cases can be mathematically derived. For a Fresnel metahologram with a phase profile of $\phi(x, y)$ for the circularly polarized light with its spin $\sigma = 1$, it generates a holographic image at the $z = z'$, where the electric field with the paraxial approximation can be expressed as [44, 93]

$$E_\sigma(x, y, z') = \frac{\exp(ikz)}{i\lambda z} \int\int A(x_0, y_0) e^{i\phi(x_0, y_0)} \exp\left\{ i \frac{k}{2z'} \left[(x - x_0)^2 + (y - y_0)^2 \right] \right\} dx_0 dy_0, \tag{4.11}$$

where the amplitude A of incident light is considered without the phase (thus $A = A^*$), $k = 2\pi/\lambda$, λ is the operating wavelength. If the same hologram is illuminated by a circularly polarized light with the other spin $\sigma = -1$, we have the electric field as

$$E_{-\sigma}(x, y, z') = \frac{\exp(ikz')}{i\lambda z'} \int\int A(x_0, y_0) e^{-i\phi(x_0, y_0)} \exp\left\{ i \frac{k}{2z'} \left[(x - x_0)^2 + (y - y_0)^2 \right] \right\} dx_0 dy_0. \tag{4.12}$$

Its relative intensity profile has the form of

$$
\begin{aligned}
&I_{-\sigma}(x, y, z) = \left|E_{-\sigma}\left(x, y, z'\right)\right|^2 = \left|E_{-\sigma}\left(x, y, z'\right)^*\right|^2 \\
&= \left|\frac{\exp\left(-ikz'\right)}{i\lambda(-z')} \int\int A^*(x_0, y_0) e^{i\phi(x_0, y_0)} \exp\left\{i\frac{k}{2(-z')}\left[(x - x_0)^2 + (y - y_0)^2\right]\right\} dx_0 dy_0\right|^2 \\
&= \left|E_{\sigma}\left(x, y, -z^{'}\right)\right|^2 = I_{-\sigma}\left(x, y, -z^{'}\right)
\end{aligned}
\tag{4.13}
$$

which means that the holographic image for the inverse spin is located at z = −z′, i.e., a virtual image.

For a Fraunhofer meta-hologram illuminated by a circularly polarized light with $\sigma = 1$, its intensity at the target plane can be expressed as [49]

$$
I_{\sigma}\left(x, y, z^{'}\right) = \frac{1}{\left(\lambda z^{'}\right)^2}\left|\int\int A(x_0, y_0) e^{i\phi(x_0, y_0)} \exp\left[-i\frac{k}{z^{'}}(x x_0 + y y_0)\right] dx_0 dy_0\right|^2. \tag{4.14}
$$

When it is illuminated by a circularly polarized light with $\sigma = -1$, the intensity profile is

$$
\begin{aligned}
&I_{-\sigma}\left(x, y, z'\right) = \frac{1}{(\lambda z')^2}\left|\int\int A(x_0, y_0) e^{-i\phi(x_0, y_0)} \exp\left[-i\frac{k}{z^{'}}(x x_0 + y y_0)\right] dx_0 dy_0\right|^2 \\
&= \frac{1}{(\lambda z')^2}\left|\int\int A^*(x_0, y_0) e^{i\phi(x_0, y_0)} \exp\left[-i\frac{k}{z^{'}}(-x x_0 - y y_0)\right] dx_0 dy_0\right|^2 = I_{\sigma}\left(-x, -y, z'\right) \\
&= \frac{1}{(\lambda z')^2}\left|\int\int A^*(x_0, y_0) e^{i\phi(x_0, y_0)} \exp\left[-i\frac{k}{-z^{'}}(x x_0 + y y_0)\right] dx_0 dy_0\right|^2 = I_{\sigma}\left(x, y, -z^{'}\right),
\end{aligned}
\tag{4.15}
$$

which means that the Fraunhofer metahologram could give two images. One is the same with the Fresnel metahologram and the other refers to a real image with centrosymmetric feature, although the Fraunhofer metahologram is observed by the second case.

In addition, when the sparse meta-holograms are introduced [15], one can realize a vectorial holographic image by combining two sparse metaholograms that generate two complementary images with the dependence of spin. Such a concept has been demonstrated at the ultra-violet region for the applications of optical vectorial anticounterfeiting [15].

4.5 Conclusions

In summary, we have discussed the chirality of light and optical metasurfaces and introduced their properties, working principles, the spin-structure interaction and applications in various fields. The involved antiferromagnetism existing in dielectric nanostructures helps us to explain the underlying physics of nanoscale halfwaveplates in terms of the well-confined electromagnetic modes, which is a good attempt to investigate and unreal the novel phenomena in nanophotonics by using classical electrodynamics. The chirality detection by using the orbital angular momentum of light is also discussed with the experimental proofs, which, we believe, will excite more interesting researches in the near future. Furthermore, the interaction between chiral light, chiral nanostructures, and macroscopic external electric and magnetic fields has not been well investigated with many unanswered problems, which might stimulate the potential applications.

References

1. G. Keiser, Optical fiber communications. Wiley Encyclopedia of Telecommunications (2003)
2. D. Gabor, A new microscopic principle. Nature **161**, 777–778 (1948)
3. E. Yablonovitch, Inhibited Spontaneous Emission in Solid-State Physics and Electronics. Phys Rev Lett **58**, 2059–2062 (1987)
4. T.W. Ebbesen, Extraordinary optical transmission through sub-wavelength hole arrays. Nature **391**, 3 (1998)
5. J.B. Pendry, Negative refraction makes a perfect lens. Phys. Rev. Lett. **85**, 3966 (2000)
6. D.R. Smith, W.J. Padilla, D.C. Vier, S.C. Nemat-Nasser, S. Schultz, Composite medium with simultaneously negative permeability and permittivity. Phys. Rev. Lett. **84**, 4184–4187 (2000)
7. S. Astilean, P. Lalanne, P. Chavel, E. Cambril, H. Launois, High-efficiency subwavelength diffractive element patterned in a high-refractive-index material for 633nm. Opt. Lett. **23**, 552–554 (1998)
8. P. Lalanne, S. Astilean, P. Chavel, E. Cambril, H. Launois, Blazed binary subwavelength gratings with efficiencies larger than those of conventional échelette gratings. Opt. Lett. **23**, 1081–1083 (1998)
9. Z. Bomzon, G. Biener, V. Kleiner, E. Hasman, Spatial Fourier-transform polarimetry using space-variant subwavelength metal-stripe polarizers. Optics Lett. **26**, 1711–1713 (2001)
10. Z. Bomzon, V. Kleiner, E. Hasman, Pancharatnam-Berry phase in space-variant polarization-state manipulations with subwavelength gratings. Opt. Lett. **26**, 1424–1426 (2001)
11. N. Yu, P. Genevet, M.A. Kats, F. Aieta, J.-P. Tetienne, F. Capasso, Z. Gaburro, Light propagation with phase discontinuities: generalized laws of reflection and refraction. Science **334**, 333–337 (2011)
12. S. Iwahashi, Y. Kurosaka, K. Sakai, K. Kitamura, N. Takayama, S. Noda, Higher-order vector beams produced by photonic-crystal lasers. Opt. Express **19**, 11963–11968 (2011)
13. L. Zhang, S. Mei, K. Huang, C.-W. Qiu, Advances in full control of electromagnetic waves with metasurfaces. Adv. Opt. Mater. **4**, 818–833 (2016)
14. H.-T. Chen, A.J. Taylor, N. Yu, A review of metasurfaces: physics and applications. Rep. Prog. Phys. **79**, 076401 (2016)
15. K. Huang, J. Deng, H.S. Leong, S.L.K. Yap, R.B. Yang, J. Teng, H. Liu, Ultraviolet metasurfaces of ≈80% efficiency with antiferromagnetic resonances for optical vectorial anti-counterfeiting. Laser & Photonics Rev. **13**, 1800289 (2019)

16. L. Huang, X. Chen, H. Mühlenbernd, G. Li, B. Bai, Q. Tan, G. Jin, T. Zentgraf, S. Zhang, Dispersionless phase discontinuities for controlling light propagation. Nano Lett. **12**, 5750–5755 (2012)
17. X. Ling, X. Zhou, K. Huang, Y. Liu, C.-W. Qiu, H. Luo, S. Wen, Recent advances in the spin Hall effect of light. Rep. Prog. Phys. **80**, 066401 (2017)
18. K.Y. Bliokh, F.J. Rodriguez-Fortuno, F. Nori, A.V. Zayats, Spin-orbit interactions of light. Nat. Photon **9**, 796–808 (2015)
19. P. Genevet, F. Capasso, Holographic optical metasurfaces: a review of current progress. Rep. Prog. Phys. **78**, 024401 (2015)
20. N. Yu, F. Capasso, Flat optics with designer metasurfaces. Nat. Mater. **13**, 139–150 (2014)
21. S.B. Glybovski, S.A. Tretyakov, P.A. Belov, Y.S. Kivshar, C.R. Simovski, Metasurfaces: From microwaves to visible. Phys. Rep. **634**, 1–72 (2016)
22. S. Kruk, Y. Kivshar, Functional meta-optics and nanophotonics governed by mie resonances. ACS Photon. **4**, 2638–2649 (2017)
23. A.E. Minovich, A.E. Miroshnichenko, A.Y. Bykov, T.V. Murzina, D.N. Neshev, Y.S. Kivshar, Functional and nonlinear optical metasurfaces. Laser Photon. Rev. **9**, 195–213 (2015)
24. Z.E. Bomzon, G. Biener, V. Kleiner, E. Hasman, Radially and azimuthally polarized beams generated by space-variant dielectric subwavelength gratings. Opt. Lett. **27**, 285–287 (2002)
25. Z. Bomzon, V. Kleiner, F. Hasman, Computer-generated space-variant polarization elements with subwavelength metal stripes. Opt. Lett. **26**, 33–35 (2001)
26. A. Niv, G. Biener, V. Kleiner, E. Hasman, Formation of linearly polarized light with axial symmetry by use of space-variant subwavelength gratings. Opt. Lett. **28**, 510–512 (2003)
27. N.A. Rubin, G. D'Aversa, P. Chevalier, Z. Shi, W.T. Chen, F. Capasso, Matrix Fourier optics enables a compact full-Stokes polarization camera. Science **365**, eaax1839 (2019)
28. W.T. Chen, A.Y. Zhu, J. Sisler, Z. Bharwani, F. Capasso, A broadband achromatic polarization-insensitive metalens consisting of anisotropic nanostructures. Nat. Commun. **10**, 355 (2019)
29. W.T. Chen, A.Y. Zhu, J. Sisler, Y.-W. Huang, K.M.A. Yousef, E. Lee, C.-W. Qiu, F. Capasso, Broadband achromatic metasurface-refractive optics. Nano Lett. **18**, 7801–7808 (2018)
30. R.C. Devlin, F. Capasso, Broadband high-efficiency dielectric metasurfaces for the visible spectrum. Proc. Natl. Acad. Sci. USA **113**, 10473 (2016)
31. F. Aieta, P. Genevet, M. Kats, F. Capasso, Aberrations of flat lenses and aplanatic metasurfaces. Opt. Express **21**, 31530–31539 (2013)
32. P. Genevet, N. Yu, F. Aieta, J. Lin, M.A. Kats, R. Blanchard, M.O. Scully, Z. Gaburro, F. Capasso, Ultra-thin plasmonic optical vortex plate based on phase discontinuities. Appl. Phys. Lett. **100**, 013101 (2012)
33. X. Chen, L. Huang, H. Muhlenbernd, G. Li, B. Bai, Q. Tan, G. Jin, C.W. Qiu, S. Zhang, T. Zentgraf, Dual-polarity plasmonic metalens for visible light. Nat. Commun. **3**, 1198 (2012)
34. M. Kim, A.M. Wong, G.V. Eleftheriades, Optical Huygens' metasurfaces with independent control of the magnitude and phase of the local reflection coefficients. Phys. Rev. X **4**, 041042 (2014)
35. M. Decker, I. Staude, M. Falkner, J. Dominguez, D.N. Neshev, I. Brener, T. Pertsch, Y.S. Kivshar, High-efficiency dielectric huygens' surfaces. Adv. Opt. Mater. **3**, 813–820 (2015)
36. C. Pfeiffer, N.K. Emani, A.M. Shaltout, A. Boltasseva, V.M. Shalaev, A. Grbic, Efficient light bending with isotropic metamaterial Huygens' surfaces. Nano Lett. **14**, 2491–2497 (2014)
37. K. Huang, H. Liu, F.J. Garcia-Vidal, M. Hong, B. Luk'yanchuk, J. Teng, C.-W. Qiu, Ultrahigh-capacity non-periodic photon sieves operating in visible light. Nat. Commun. **6**, 7059 (2015)
38. K. Huang, H. Liu, G. Si, Q. Wang, J. Lin, J. Teng, Photon-nanosieve for ultrabroadband and large-angle-of-view holograms. Laser Photon. Rev. **11**, 1700025 (2017)
39. S. Mei, M.Q. Mehmood, S. Hussain, K. Huang, X. Ling, S.Y. Siew, H. Liu, J. Teng, A. Danner, C.-W. Qiu, Flat helical nanosieves. Adv. Fun. Mater. **26**, 5255–5262 (2016)
40. J. Li, G. Si, H. Liu, J. Lin, J. Teng, K. Huang, Resonance-free ultraviolet metaoptics via photon nanosieves. Opt. Lett. **44**, 3418–3421 (2019)
41. D. Attwood, A. Sakdinawat, *X-rays and Extreme Ultraviolet Radiation: Principles and Applications* (Cambridge University Press, 2017)

42. A. Arbabi, Y. Horie, M. Bagheri, A. Faraon, Dielectric metasurfaces for complete control of phase and polarization with subwavelength spatial resolution and high transmission. Nat. Nanotechnol. **10**, 937–943 (2015)
43. G. Zheng, H. Mühlenbernd, M. Kenney, G. Li, T. Zentgraf, S. Zhang, Metasurface holograms reaching 80% efficiency. Nat. Nanotechnol. **10**, 308–312 (2015)
44. K. Huang, Z. Dong, S. Mei, L. Zhang, Y. Liu, H. Liu, H. Zhu, J. Teng, B. Luk'yanchuk, J.K. Yang, C. Qiu, Silicon multi-meta-holograms for the broadband visible light. Laser Photon. Rev. **10**, 500–509 (2016)
45. M. Khorasaninejad, W.T. Chen, R.C. Devlin, J. Oh, A.Y. Zhu, F. Capasso, Metalenses at visible wavelengths: Diffraction-limited focusing and subwavelength resolution imaging. Science **352**, 1190–1194 (2016)
46. K. Huang, F. Qin, H. Liu, H. Ye, C.W. Qiu, M. Hong, B. Luk'yanchuk, J. Teng, Planar diffractive lenses: fundamentals, functionalities, and applications. Adv. Mater. **30**, 1704556 (2018)
47. L. Huang, X. Chen, H. Mühlenbernd, H. Zhang, S. Chen, B. Bai, Q. Tan, G. Jin, K.-W. Cheah, C.-W. Qiu, J. Li, T. Zentgraf, S. Zhang, Three-dimensional optical holography using a plasmonic metasurface. Nat. Commun. **4**, 2808 (2013)
48. X. Ni, A.V. Kildishev, V.M. Shalaev, Metasurface holograms for visible light. Nat. Commun. **4** (2013)
49. D. Wen, F. Yue, G. Li, G. Zheng, K. Chan, S. Chen, M. Chen, K.F. Li, P.W.H. Wong, K.W. Cheah, E. Yue Bun Pun, S. Zhang, X. Chen, Helicity multiplexed broadband metasurface holograms. Nat. Commun. **6**, 8241 (2015)
50. W. Ye, F. Zeuner, X. Li, B. Reineke, S. He, C.-W. Qiu, J. Liu, Y. Wang, S. Zhang, T. Zentgraf, Spin and wavelength multiplexed nonlinear metasurface holography. Nat. Commun. **7**, 11930 (2016)
51. K. Huang, H. Liu, S. Restuccia, M.Q. Mehmood, S. Mei, D, Giovannini, A. Danner, M.J. Padgett, J. Teng, C.-W. Qiu, Spiniform phase-encoded metagratings entangling arbitrary rational-order orbital angular momentum. Light: Sci. Appl. **7**, 17156 (2018)
52. D. Sell, J. Yang, S. Doshay, R. Yang, J.A. Fan, Large-angle, multifunctional metagratings based on freeform multimode geometries. Nano Lett. **17**, 3752–3757 (2017)
53. Y. Ra'di, D.L. Sounas, A. Alu, Metagratings: Beyond the limits of graded metasurfaces for wave front control. Phys. Rev. Lett. **119**, 067404 (2017)
54. A. Pors, M.G. Nielsen, S.I. Bozhevolnyi, Plasmonic metagratings for simultaneous determination of Stokes parameters. Optica **2**, 716–723 (2015)
55. M. Khorasaninejad, K.B. Crozier, Silicon nanofin grating as a miniature chirality-distinguishing beam-splitter. Nat. Commun. **5**, 5386 (2014)
56. M. Papaioannou, E. Plum, N.I. Zheludev, All-optical pattern recognition and image processing on a metamaterial beam splitter. ACS Photon. **4**, 217–222 (2017)
57. C. Huang, C. Zhang, S. Xiao, Y. Wang, Y. Fan, Y. Liu, N. Zhang, G. Qu, H. Ji, J. Han, L. Ge, Y. Kivshar, Q. Song, Ultrafast control of vortex microlasers. Science **367**, 1018–1021 (2020)
58. Y. Yang, W. Wang, P. Moitra, I.I. Kravchenko, D.P. Briggs, J. Valentine, Dielectric meta-reflectarray for broadband linear polarization conversion and optical vortex generation. Nano Lett. **14**, 1394–1399 (2014)
59. A. Arbabi, E. Arbabi, Y. Horie, S.M. Kamali, A. Faraon, Planar metasurface retroreflector. Nat. Photon. **11**, 415–420 (2017)
60. F. Yesilkoy, E.R. Arvelo, Y. Jahani, M. Liu, A. Tittl, V. Cevher, Y. Kivshar, H. Altug, Ultrasensitive hyperspectral imaging and biodetection enabled by dielectric metasurfaces. Nat. Photon. **13**, 390–396 (2019)
61. J. Zhou, H. Qian, C.-F. Chen, J. Zhao, G. Li, Q. Wu, H. Luo, S. Wen, Z. Liu, Optical edge detection based on high-efficiency dielectric metasurface. Proc. Natl. Acad. Sci. 201820636 (2019)
62. P. Berto, L. Philippet, J. Osmond, C.F. Liu, A. Afridi, M. Montagut Marques, B. Molero Agudo, G. Tessier, R. Quidant, Tunable and free-form planar optics. Nat. Photon. **13**, 649–656 (2019)
63. S.-Q. Li, X. Xu, R. Maruthiyodan Veetil, V. Valuckas, R. Paniagua-Domínguez, A.I. Kuznetsov, Phase-only transmissive spatial light modulator based on tunable dielectric metasurface. Science **364**, 1087–1090 (2019)

64. C. Zou, A. Komar, S. Fasold, J. Bohn, A.A. Muravsky, A.A. Murauski, T. Pertsch, D.N. Neshev, I. Staude, Electrically tunable transparent displays for visible light based on dielectric metasurfaces. ACS Photon. (2019)
65. R.A. Maniyara, D. Rodrigo, R. Yu, J. Canet-Ferrer, D.S. Ghosh, R. Yongsunthon, D.E. Baker, A. Rezikyan, F.J. García de Abajo, V. Pruneri, Tunable plasmons in ultrathin metal films. Nat. Photon. (2019)
66. E. Arbabi, A. Arbabi, S.M. Kamali, Y. Horie, M. Faraji-Dana, A. Faraon, MEMS-tunable dielectric metasurface lens. Nat. Commun. **9**, 812 (2018)
67. Y.-W. Huang, H.W.H. Lee, R. Sokhoyan, R.A. Pala, K. Thyagarajan, S. Han, D.P. Tsai, H.A. Atwater, Gate-tunable conducting oxide metasurfaces. Nano Lett. **16**, 5319–5325 (2016)
68. D. Franklin, Y. Chen, A. Vazquez-Guardado, S. Modak, J. Boroumand, D. Xu, S.-T. Wu, D. Chanda, Polarization-independent actively tunable colour generation on imprinted plasmonic surfaces. Nat. Commun. **6** (2015)
69. J. Lin, J.P.B. Mueller, Q. Wang, G. Yuan, N. Antoniou, X.-C. Yuan, F. Capasso, Polarization-controlled tunable directional coupling of surface plasmon polaritons. Science **340**, 331–334 (2013)
70. L. Allen, M. Padgett, M. Babiker, The orbital angular momentum of light. Progress Optics: Vol XXXIX **39**, 291–372 (1999)
71. H.A. Haus, *Waves and Fields in Optoelectronics*, vol. 1 (Prentice-Hall Englewood Cliffs, NJ, 1984).
72. L. Allen, M. Beijersbergen, R. Spreeuw, J. Woerdman, Orbital angular momentum of light and the transformation of Laguerre-Gaussian laser modes. Phys. Rev. A **45**, 8185–8189 (1992)
73. Y. Tang, A.E. Cohen, Optical chirality and its interaction with matter. Phys. Rev. Lett. **104**, 163901 (2010)
74. K.Y. Bliokh, F. Nori, Characterizing optical chirality. Phys. Rev. A **83**, 021803 (2011)
75. X. Zambrana-Puyalto, X. Vidal, G. Molina-Terriza, Angular momentum-induced circular dichroism in non-chiral nanostructures. Nat. Commun. **5**, 1–7 (2014)
76. A. Mair, A. Vaziri, G. Weihs, A. Zeilinger, Entanglement of the orbital angular momentum states of photons. Nature **412**, 313–316 (2001)
77. J. Wang, J.-Y. Yang, I.M. Fazal, N. Ahmed, Y. Yan, H. Huang, Y. Ren, Y. Yue, S. Dolinar, M. Tur, Terabit free-space data transmission employing orbital angular momentum multiplexing. Nat. Photon. **6**, 488–496 (2012)
78. N. Bozinovic, Y. Yue, Y. Ren, M. Tur, P. Kristensen, H. Huang, A.E. Willner, S. Ramachandran, Terabit-scale orbital angular momentum mode division multiplexing in fibers. Science **340**, 1545–1548 (2013)
79. L. Gong, Q. Zhao, H. Zhang, X.-Y. Hu, K. Huang, J.-M. Yang, Y.-M. Li, Optical orbital-angular-momentum-multiplexed data transmission under high scattering. Light: Sci. Appl. **8**, 27 (2019)
80. W. Löffler, D. Broer, J. Woerdman, Circular dichroism of cholesteric polymers and the orbital angular momentum of light. Phys. Rev. A **83**, 065801 (2011)
81. M. Babiker, C.R. Bennett, D.L. Andrews, L.C. Dávila Romero, Orbital angular momentum exchange in the interaction of twisted light with molecules. Phys. Rev. Lett. **89**, 143601 (2002)
82. W. Brullot, M.K. Vanbel, T. Swusten, T. Verbiest, Resolving enantiomers using the optical angular momentum of twisted light. Sci. Adv. **2** (2016)
83. J. Ni, Z. Wang, Z. Lao, Y. Hu, K. Huang, S. Ji, J. Li., Z. Huang. D. Wu, C. Qiu, Ultra-sensitive experimental detection of chiral meso-structures by orbital angular momentum of light. arXiv preprint arXiv:1809.02754 (2018)
84. F. Monticone, N.M. Estakhri, A. Alù, Full control of nanoscale optical transmission with a composite metascreen. Phys. Rev. Lett. **110**, 203903 (2013)
85. T. Cai, G. Wang, S. Tang, H. Xu, J. Duan, H. Guo, F. Guan, S. Sun, Q. He, L. Zhou, High-efficiency and full-space manipulation of electromagnetic wave fronts with metasurfaces. Phys. Rev. Appl. **8**, 034033 (2017)
86. L. Kipp, M. Skibowski, R.L. Johnson, R. Berndt, R. Adelung, S. Harm, R. Seemann, Sharper images by focusing soft X-rays with photon sieves. Nature **414**, 184–188 (2001)

87. M. Mehmood, S. Mei, S. Hussain, K. Huang, S. Siew, L. Zhang, T. Zhang, X. Ling, H. Liu, J. Teng, Visible-frequency metasurface for structuring and spatially multiplexing optical vortices. Adv. Mater. **28**, 2533–2539 (2016)
88. L. Drescher, O. Kornilov, T. Witting, G. Reitsma, N. Monserud, A. Rouzée, J. Mikosch, M.J.J. Vrakking, B. Schütte, Extreme-ultraviolet refractive optics. Nature **564**, 91–94 (2018)
89. S. Wang, P.C. Wu, V.-C. Su, Y.-C. Lai, M.-K. Chen, H.Y. Kuo, B.H. Chen, Y.H. Chen, T.-T. Huang, J.-H. Wang, R.-M. Lin, C.-H. Kuan, T. Li, Z. Wang, S. Zhu, D.P. Tsai, A broadband achromatic metalens in the visible. Nat. Nanotechnol. **13**, 227–232 (2018)
90. A. Arbabi, E. Arbabi, S.M. Kamali, Y. Horie, S. Han, A. Faraon, Miniature optical planar camera based on a wide-angle metasurface doublet corrected for monochromatic aberrations. Nat. Commun. **7**, 13682 (2016)
91. W.T. Chen, A.Y. Zhu, V. Sanjeev, M. Khorasaninejad, Z. Shi, E. Lee, F. Capasso, A broadband achromatic metalens for focusing and imaging in the visible. Nat. Nanotechnol. **13**, 220–226 (2018)
92. X. Ling, X. Zhou, X. Yi, W. Shu, Y. Liu, S. Chen, H. Luo, S. Wen, Fan, D.: Giant photonic spin Hall effect in momentum space in a structured metamaterial with spatially varying birefringence. Light: Sci. Appl. **4**, e290 (2015)
93. K. Huang, H.F. Gao, G.W. Cao, P. Shi, X.B. Zhang, Y. Li , Design of DPE for modulating the electric field at the out-of-focus plane in a lens system. Appl. Opt. **51**, 5149–5153 (2012)